



Tuning single-photon sources for telecom multi-photon experiments

CHIARA GREGANTI,¹ PETER SCHIANSKY,¹ IRATI ALONSO CALAFELL,¹ LORENZO M. PROCOPIO,² LEE A. ROZEMA,¹ AND PHILIP WALTHER¹

¹Vienna Center for Quantum Science and Technology (VCQ), Faculty of Physics, University of Vienna, Boltzmannngasse 5, 1090 Vienna, Austria

²Centre de Nanosciences et de Nanotechnologies C2N, CNRS, Université Paris-Saclay, Route de Nozay, 91460 Marcoussis, France

*chiara.greganti@univie.ac.at

Abstract: Multi-photon state generation is of great interest for near-future quantum simulation and quantum computation experiments. To-date spontaneous parametric down-conversion is still the most promising process, even though two major impediments still exist: accidental photon noise (caused by the probabilistic non-linear process) and imperfect single-photon purity (arising from spectral entanglement between the photon pairs). In this work, we overcome both of these difficulties by (1) exploiting a passive temporal multiplexing scheme and (2) carefully optimizing the spectral properties of the down-converted photons using periodically-poled KTP crystals. We construct two down-conversion sources in the telecom wavelength regime, finding spectral purities of > 91%, while maintaining high four-photon count rates. We use single-photon grating spectrometers together with superconducting nanowire single-photon detectors to perform a detailed characterization of our multi-photon source. Our methods provide practical solutions to produce high-quality multi-photon states, which are in demand for many quantum photonics applications.

Published by The Optical Society under the terms of the [Creative Commons Attribution 4.0 License](https://creativecommons.org/licenses/by/4.0/). Further distribution of this work must maintain attribution to the author(s) and the published article's title, journal citation, and DOI.

OCIS codes: (270.5585) Quantum information and processing; (270.4180) Multiphoton processes.

References and links

1. X.-L. Wang, L.-K. Chen, W. Li, H.-L. Huang, C. Liu, C. Chen, Y.-H. Luo, Z.-E. Su, D. Wu, Z.-D. Li, H. Lu, Y. Hu, X. Jiang, C.-Z. Peng, L. Li, N.-L. Liu, Y.-A. Chen, C.-Y. Lu, and J.-W. Pan, "Experimental ten-photon entanglement," *Phys. Rev. Lett.* **117**(21), 210502 (2016).
2. H. Wang, Y. He, Y.-H. Li, Z.-E. Su, B. Li, H.-L. Huang, X. Ding, M.-C. Chen, C. Liu, J. Qin, J.-P. Li, Y.-M. He, C. Schneider, M. Kamp, C.-Z. Peng, S. Hoefling, C.-Y. Lu, and J.-W. Pan, "High-efficiency multiphoton boson sampling," *Nat. Photon.* **11**, 361 (2017).
3. M. J. Hartmann, "Quantum simulation with interacting photons," *J. Opt.* **18**, 104005 (2016).
4. E. Meyer-Scott, N. Montaut, J. Tiedau, L. Sansoni, H. Herrmann, T. J. Bartley, and C. Silberhorn, "Limits on the heralding efficiencies and spectral purities of spectrally filtered single photons from photon-pair sources," *Phys. Rev. A* **95**(6), 061803 (2017).
5. F. Laudenbach, H. Hübel, M. Hentschel, P. Walther, and A. Poppe, "Modelling parametric down-conversion yielding spectrally pure photon pairs," *Opt. Express* **24**(3), 2712–2727 (2016).
6. D.C. Burnham and D.L. Weinberg, "Observation of simultaneity in parametric production of optical photon pairs," *Phys. Rev. Lett.* **25**(2), 84–87 (1970).
7. F. Laudenbach, R.-B. Jin, C. Greganti, M. Hentschel, P. Walther, and H. Huebel, "Numerical investigation of photon-pair generation in periodically poled MTiOXO4 (M = K, Rb, Cs; X = P, As) crystals," *Phys. Rev. A* **8**(2), 024035 (2017).
8. P. B. Dixon, J. H. Shapiro, and F. N. C. Wong, "Spectral engineering by gaussian phase-matching for quantum photonics," *Opt. Express* **21**(5), 5879–5890 (2013).
9. A. Dosseva, L. Cincio, and A. M. Brańczyk, "Shaping the joint spectrum of down-converted photons through optimized custom poling," *Phys. Rev. A* **93**(1), 013801 (2016).
10. R. H. Hadfield and G. Johansson, *Superconducting Devices in Quantum Optics* (Springer Verlag, 2016).

11. N. C. Harris, D. Bunandar, M. Pant, G. R. Steinbrecher, J. Mower, M. Prabhu, T. Baehr-Jones, M. Hochberg, and D. Englund, "Large-scale quantum photonic circuits in silicon," *Nanophotonics* **5**(3), 456–468 (2016).
12. J. W. Silverstone, D. Bonneau, J. L. O'Brien, and M. G. Thompson, "Silicon quantum photonics," *IEEE J. Sel. Top. Quantum Electron.* **22**(6), 390–402 (2016).
13. F. Kaneda, F. Xu, J. Chapman, P. G. Kwiat, "Quantum-memory-assisted multi-photon generation for efficient quantum information processing," *Optica* **4**(9), 1034–1037 (2017).
14. R. B. Jin, R. Shimizu, K. Wakui, H. Benichi, and M. Sasaki, "Widely tunable single photon source with high purity at telecom wavelength," *Opt. Express* **21**(9), 10659–10666 (2013).
15. N. Bruno, A. Martin, T. Guerreiro, B. Sanguinetti, and R. T. Thew, "Pulsed source of spectrally uncorrelated and indistinguishable photons at telecom wavelengths," *Opt. Express* **22**(14), 17246–17253 (2014).
16. T. Gerrits, F. Marsili, V. B. Verma, L. K. Shalm, M. Shaw, R. P. Mirin, and S. W. Nam, "Spectral correlation measurements at the Hong-Ou-Mandel interference dip," *Phys. Rev. A* **91**(1), 013830 (2015).
17. M. M. Weston, H. M. Chrzanowski, S. Wollmann, A. Boston, J. Ho, L. K. Shalm, V. B. Verma, M. S. Allman, S. W. Nam, R. B. Patel, S. Slussarenko, and G. J. Pryde, "Efficient and pure femtosecond-pulse-length source of polarization-entangled photons," *Opt. Express* **24**(10), 10869–10879 (2016).
18. F. Kaneda, K. Garay-Palmett, A. B. U'Ren, and P. G. Kwiat, "Heralded single-photon source utilizing highly nondegenerate, spectrally factorable spontaneous parametric downconversion," *Opt. Express* **24**(10), 10733–10747 (2016).
19. R. B. Jin, M. Fujiwara, T. Yamashita, S. Miki, Hirota Terai, Z. Wang, K. Wakui, R. Shimizu, M. Sasaki, "Efficient detection of a highly bright photon source using superconducting nanowire single photon detectors," *Opt. Commun.* **336**, 47–54 (2015).
20. M. A. Broome, M. P. Almeida, A. Fedrizzi, and A. G. White, "Reducing multi-photon rates in pulsed down-conversion by temporal multiplexing," *Opt. Express* **19**(23), 22698–22708 (2011).
21. R. B. Jin, R. Shimizu, I. Morohashi, K. Wakui, M. Takeoka, S. Izumi, T. Sakamoto, M. Fujiwara, T. Yamashita, S. Miki, H. Terai, Z. Whang, and M. Sasaki, "Efficient generation of twin photons at telecom wavelengths with 2.5 GHz repetition-rate-tunable comb laser," *Sci. Rep.* **4**, 7468 (2014).
22. X.-S. Ma, S. Zotter, J. Kofler, T. Jennewein, and A. Zeilinger, "Experimental generation of single photons via active multiplexing," *Phys. Rev. A* **83**(4), 043814 (2011).
23. E. A. B. Saleh and M. C. Teich, *Fundamentals of photonics, 2nd ed.*, Chap. 21 (Wiley, 2007).
24. P. J. Mosley, J. S. Lundeen, B. J. Smith, and I. A. Walmsley, "Conditional preparation of single photons using parametric downconversion: a recipe for purity," *New J. Phys.* **10**, 093011 (2008).
25. C. K. Hong, Z. Y. Ou and L. Mandel, "Measurement of subpicosecond time intervals between two photons by interference," *Phys. Rev. Lett.* **59**(18), 2044–2046 (1987).
26. C. I. Osorio, N. Sangouard, and R. T. Thew, "On the purity and indistinguishability of down-converted photons," *J. Phys. B: At. Mol. Opt. Phys.* **46**, 055501 (2012).
27. We remind that the HOM visibility of two photons from independent sources is given by the heralded coincidences (equivalent to the four-fold coincidence events) as $V = 1 - CC_{min}/CC_{max}$, with CC_{min} the average coincidences when the two photons are indistinguishable (zero time delay, quantum case) and CC_{max} the average coincidences when they are fully distinguishable (far apart in time, classical case).
28. W. Heisenberg, "Über den anschaulichen Inhalt der quantentheoretischen Kinematik und Mechanik / The actual content of quantum theoretical kinematics and mechanics," *Z. Phys.* **43**(3–4), 172 (1927).
29. A. Fedrizzi, T. Herbst, M. Aspelmeyer, M. Barbieri, T. Jennewein, and A. Zeilinger, "Anti-symmetrization reveals hidden entanglement," *New J. Phys.* **11**, 103052 (2009).
30. C. Chen, C. Bo, M. Y. Niu, F. Xu, Z. Zhang, J. H. Shapiro, and F. N. Wong, "Efficient generation and characterization of spectrally factorable biphotons," *Opt. Express* **25**(7), 7300–7312 (2017).
31. K. Fradkin, A. Arie, A. Skliar, and G. Rosenman, "Tunable midinfrared source by difference frequency generation in bulk periodically poled KTiOPO4," *Appl. Phys. Lett.* **74**(7), 914–916 (1999).
32. F. König and F. N. C. Wong, "Extended phase matching of second-harmonic generation in periodically poled KTiOPO4 with zero group velocity mismatch," *Appl. Phys. Lett.* **84**(10), 1644 (2004).
33. S. Emanueli and A. Arie, "Temperature-dependent dispersion equations for KTiOPO4 and KTiOAsO4," *Appl. Opt.* **42**(33), 6661–6665 (2003).
34. F. Laudenbach, H. Huebel, M. Hentschel, and A. Poppe, "QPMoptics: a novel tool to simulate and optimise photon pair creation," in *Proceedings of SPIE Photonics Europe 2016* (International Society for Optics and Photonics, Brussels, 2016), pp. 98940V.

1. Introduction

Real-world quantum applications will require almost-ideal quantum technologies. Photonic systems are an extremely promising resource for near-term quantum applications requiring multi-qubit states, such as boson sampling and quantum simulation [1–3]. In particular, single-photon sources based on spontaneous parametric down-conversion (SPDC) are continually

being engineered to obtain probabilistic and even quasi-deterministic generation of high-quality single photons [4, 5]. The SPDC process, first demonstrated in the 1970s [6], is still enriched by the investigation of different non-linear crystals [7] as well as by new methods of crystal-fabrication [8, 9]. These sorts of studies have enabled efficient detection and near-lossless manipulation of single photons in the telecom-wavelength regime [10–13], providing a set of tools which are a prerequisite for long distance quantum communication. Although photon-pair sources have been greatly improved over the past few years [14–19], enhancements are still needed for multi-photon applications. Here we present an experimental characterization of two periodically-poled potassium titanyl phosphate (ppKTP) photon-pairs sources, and study their application to multi-photon experiments. To generate our multi-qubit states we use degenerate SPDC, allowing us to use both the signal and the idler photons as qubits. With our sources we generate high purity multi-photon states with high count rates at telecom wavelengths.

The important characteristics of a single-photon source for quantum information experiments are the brightness, the purity of the generated photons, and the heralding efficiency. The brightness is the detected photon-count rate at a fixed pump power (usually expressed in Hz/mW); the purity quantifies the degree to which the photon pairs are uncorrelated, i.e. the indistinguishability of the down-converted photons; and the heralding efficiency represents the detection efficiency of one photon conditioned on the detection of the second photon (often called the trigger photon). All of these three features cannot be optimised simultaneously in the same configuration, and it is thus necessary to make a trade-off for each specific application. For multi-photon experiments (wherein different SPDC sources are probabilistically combined) the two most important parameters are the brightness and the purity. Typically, increasing the brightness leads to noise from the higher-order terms present in the SPDC process. To minimise this noise we use a passive temporal multiplexing scheme [20]. This enables us to increase the pump power for the down-conversion process while keeping the probability of higher-order emissions low. The single-photon purity is primarily governed by spectral correlations between the signal and idler photons. We quantify it in two ways. First, we perform correlated measurements of the down-converted photons' wavelength using single-photon grating spectrometers. Secondly, we indirectly measure it by performing quantum interference measurements between different photons.

In this work we present a detailed study optimising the purity and the brightness. While many of the parameters we consider have been individually studied, they have not been simultaneously optimized. Here we show that by tuning a wide variety of parameters can result in a near-optimal configuration to produce high-quality photons. We study the effect of filtering the down-converted photons, tuning the pump laser (its centre wavelength and pulse width), and changing the crystal phase-matching properties (by changing the crystal temperature). The rest of the work is divided as follows: the first section presents the theoretical background used to simulate and design our experiment; the second section introduces the experimental details; and the third section presents the measurement data and analysis.

2. Theory

2.1. Temporal multiplexing scheme

The $2n$ -fold coincidence rate, corresponding to detecting n -photon pairs, for pulsed SPDC sources can be written in terms of the probability of generating a photon pair per pulse (μ), the repetition rate of the pump laser (RR), and the total detection efficiency (η) [21]: $C_{2n} = RR \cdot \mu^n \cdot \eta^{2n}$. Increasing the pump power, and consequently μ , results in high n -photon count rates, at the cost of also increasing the higher-order ($n + 1$ and higher) terms of SPDC. These components will considerably degrade any multi-photon interference. In order to maintain a high brightness for the n -photon terms, while simultaneously keeping the noise from the $(n + 1)$ terms low, we

implement a passive temporal multiplexing scheme [20]. This approach increases the repetition rate of the pump laser and decreases the power of each pulse. In this way it reduces the multi-pair emission by a factor corresponding to the increase of the repetition rate. Specifically they are reduced by a factor of $\frac{1}{m^{(n-1)}}$, where $m = 2^k$, k is the number of time the repetition rate is doubled and n is the number of photon pairs emitted. To do this experimentally, the pump beam is split in two different physical paths. The second path is lengthened with respect to the first path, in order to delay the pump by half of the initial pulse period. The two beams are then recombined into a single path, doubling the original repetition rate (see Fig. 1). In principle, this procedure can be iterated to achieve arbitrarily high repetition rates; however, in practice, the jitter and dead time of the detectors limit this.

It is worth noting that similar performance enhancements can be achieved by utilising a spatial multiplexing scheme [22]. In this case, the pump laser is split into different path modes and not recombined, but a different source is built in each path. This requires additional non-linear crystals and collection optics. In our scheme, we do not need these additional elements.

2.2. Joint spectral intensity

The SPDC process in a periodically-poled crystal with poling period Λ at temperature T must satisfy energy and momentum conservation:

$$\omega_p = \omega_s + \omega_i, \quad \omega_p n_p(\omega_p, T) = \omega_s n_s(\omega_s, T) + \omega_i n_i(\omega_i, T) + 2\pi c \frac{m}{\Lambda(T)}, \quad (1)$$

where the subscripts s, i, p denote signal, idler and pump photons, respectively, ω_x and n_x are the respective angular frequencies and refractive indices with $x = \{p, s, i\}$, c is the speed of light and m is the quasi phase matching (QPM) order [23].

The two-photon state can be expressed as

$$|\Psi\rangle = N \chi_{\text{eff}}^{(2)} L \int d\omega_s d\omega_i f(\omega_s, \omega_i) a_s^\dagger(\omega_s) a_i^\dagger(\omega_i) |0\rangle, \quad (2)$$

where a_x^\dagger are the respective creation operators, L is the crystal length, $\chi_{\text{eff}}^{(2)}$ is the effective second-order non-linearity of the crystal, N is a proper normalization constant, and f is the joint spectral amplitude (JSA). The JSA function fully characterizes the spectral properties of the two-photon state and is the product of the pump envelope amplitude (α) and phase matching amplitude (ϕ). In general the pump envelope α can be approximated by a gaussian function, which describes many laser systems. For our work, however, we use a sech function, as this matches our experimentally measured spectra better, see Section 4.2. (This subtlety is important in order to optimally tune the spectral properties of our single-photon sources.) We use the following forms of α and ϕ :

$$\alpha(\omega_s, \omega_i) = \text{sech} \left((\omega_s + \omega_i - \omega_p) \cdot \frac{2 \text{arccosh} \sqrt{2}}{\Delta\omega_p} \right) \quad (3a)$$

$$\phi(\omega_s, \omega_i) = \exp \left(\frac{i\Delta k L}{2} \right) \text{sinc} \left(\frac{\Delta k L}{2} \right) \quad (3b)$$

where $\Delta\omega_p$ is the FWHM of the pump pulse and $\Delta k = (k_s + k_i + 2\pi c \frac{m}{\Lambda} - k_p)$ is the difference between the wavevectors. The width of α is proportional to the bandwidth of the pump photons, and the width of ϕ is inverse proportional to the length of the crystal.

The spectral purity of an individual photon degrades when the JSA contains spectral correlations between the photon pairs. These correlations can be analysed using a Schmidt

decomposition of the JSA, $f(\omega_s, \omega_i) = \sum_k c_k r_k(\omega_s) s_k(\omega_i)$, where c_k are the Schmidt-coefficients, and $\{r_k(\omega)\}$ and $\{s_k(\omega)\}$ are two orthogonal spectral basis sets. If the JSA is separable, then the two photons are fully uncorrelated. This condition is necessary to produce high-quality spectrally pure single photons. The spectral purity can be extracted from the Schmidt decomposition as $P_{JSA} = \sum_k c_k^4$, which is the inverse of the Schmidt number $K_{JSA} = 1/\sum_k c_k^4$ [24].

In actual measurements, the phases appearing in the JSA are difficult to detect. Thus in practice intensity distributions (JSI) are measured. In our work, we compute the spectral purity from the Schmidt decomposition of the JSI (P_{JSI}, K_{JSI}). This neglects relative phases information which could affect the purities. Thus we perform additional tests.

2.3. Hong-Ou-Mandel interference

In order to fully reconstruct the spectral purity, a complementary method is to directly interfere the two photons via a Hong-Ou-Mandel (HOM) experiment [25]. Here the spectral purity of the two photons is connected to the visibility V of the HOM dip. Consider two states ρ_A and ρ_B (where $\rho_A = \text{Tr}_B [|\Psi\rangle\langle\Psi|]$) with respective purities P_A and P_B (where $P = \text{Tr} [\rho^2]$). It is also common to introduce the indistinguishability, which is connected to the operational distance ρ_A and ρ_B , $D(\rho_A, \rho_B) = \|\rho_A - \rho_B\|^2$ (where $\|\cdot\|$ is the Frobenius norm). With these definitions, the HOM visibility can be written as

$$V = \frac{P_A + P_B - D(\rho_A, \rho_B)}{2}. \quad (4)$$

While the two purities are properties of the single photons, the indistinguishability is a joint property of two (or more) photons. If a HOM experiment is performed on a photon pair created in the same event $D(\rho_A, \rho_B) \neq 0$, and the visibility cannot be used to directly extract the single-photon purities. Rather, it provides the access to the indistinguishability and allows one to analyse the symmetry of the JSA under exchange of signal and idler photons [26]. On the other hand, measuring the HOM visibility of two signal (or two idler) photons from two identical but independent sources [27] (or from the same source but from different pulses) yields $D = 0$, and thus allows one to extract the single-photon purities.

3. Experimental scheme

Our experimental setup is composed of two nominally identical single-photon sources (Source 1 and Source 2) to generate collinear SPDC in the telecom C-band, see Fig. 1(a). Each source consists of a ppKTP crystal, with a length of 30 mm, a poling period of 46.2 μm , and a tunable temperature T . The crystals are pumped by a mode-locked laser with a repetition rate (RR) of 76 MHz, a tunable central wavelength centred around 775 nm, and a tunable pulse width centred around 2 ps. Ultra-narrow bandpass filters with a full width at half maximum (FWHM) bandwidth of 3.2 nm and an almost top-hat shape transmittivity are used to further improve the photons' purity, see Section 4.4.

A passive temporal multiplexing scheme based on four beam splitters enables us to set the laser RR to [76, 152, 304, 608] MHz (Fig. 1(b)).

We use four superconducting nanowire single-photon detectors (SNSPDs) from Photon Spot to detect the single photons. The detectors operate at a temperature of 0.9 K, and have an average system detection efficiency of 0.80, a jitter time of 300 ps, and a dead time of 80 ns. The coincidence events are collected using an AIT TTM8000 time tagging module within a coincidence window of 1 ns to avoid detecting photons from consecutively emitted pairs at high RR .

In order to analyse the single-photon spectra we employed a home-built single-photon scanning

monochromator, which is fiber coupled (and thus detector-independent) and has a resolution of 0.12 nm and a transmission efficiency of 0.3. More details can be found in Appendix 5.1.

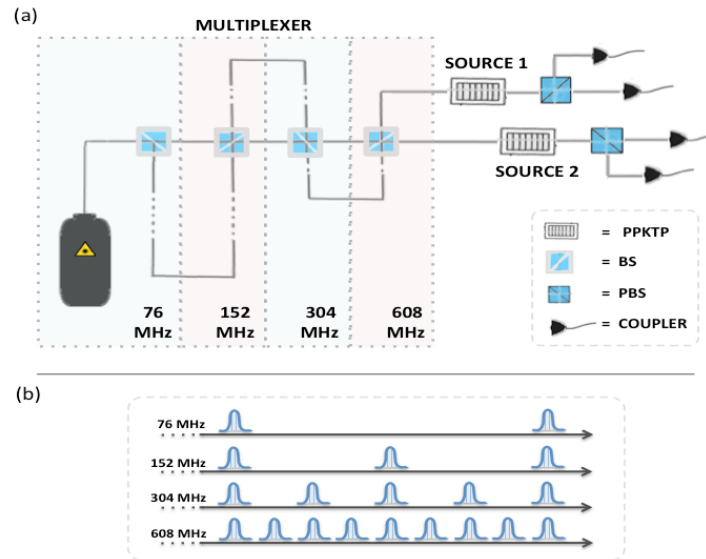


Fig. 1. (a) Two ppKTP single-photon sources are pumped by a ps-pulsed laser with a repetition rate of 76 MHz. A multiplexing scheme, which splits and recombines the pump beam via beam splitters (BS), increases the repetition rate to a maximum of 608 MHz. The down-converted signal and idler photons are separated by polarizing beamsplitters (PBS) and coupled into single-mode fibers, which can be directed to one of our various detection apparatus. (b) A cartoon of the doubling of the repetition rate of the laser.

4. Results

4.1. Photon count rate versus repetition rate

In order to analyse the brightness of the sources, we acquire 2-fold coincidence events from a single source (Fig. 2(a)) and 4-fold coincidence events from the two independent sources (Fig. 2(b)) at different RR of the pump laser. As expected, the 2-fold rate increases linearly with the pump power, and the 4-fold rate increases quadratically with the pump power. In general, the n -fold is proportional to the pulse power (and therefore μ) to the power of n . The SNSPDs have quantum efficiencies of 0.82 and 0.88 for Source 1 and 0.75 and 0.72 for Source 2. Due to technical issues, one of the detectors saturates at high count rates. We compensate for this by decreasing the current bias of that detector at high count rates, which unfortunately also lowers the system detection efficiency. The final data point at high power and 608 MHz (shown in purple) was taken in this configuration (with a system detection efficiency equal to 0.57) and then renormalized to be comparable with the rest of the data. At a power of 440 mW we obtain a 2-fold coincidence rate of 1.3 MHz, corresponding to a brightness of 2.9 kHz/mW, and a 4-fold coincidence rate of 1.5 kHz with a $RR = 608$ MHz. We underline that even at max RR , the counts remain stable over weeks, as the temporal multiplexing scheme is composed by simple passive optical elements which require standard laboratory-temperature conditions.

In order to quantify the multi-photon noise (called accidental coincidences), which, in this specific case, consists of the 4-fold coincidences contribution coming from higher-order emissions of each SPDC source, we split the path of each signal photon in two paths and reconnect to two

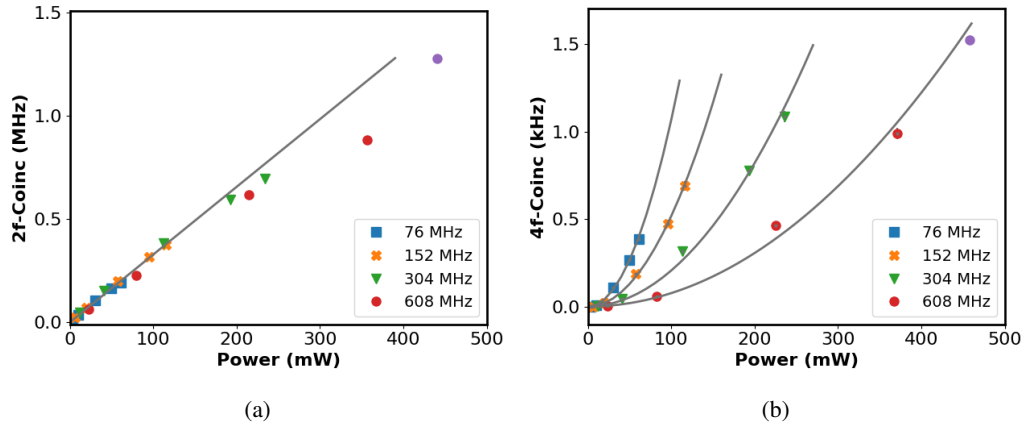


Fig. 2. Count rates of 2-fold coincidences (a) and 4-fold coincidences (b) from one and two independent sources, respectively, at different repetition rates. The purple dots correspond to renormalized data points at 608 MHz (for more details see main text). The error bars, based on Poissonian statistics, in (a) are smaller than the dots size.

distinct SPNSDs. In this way blocking one signal photon at a time, we are able to measure a partial amount of the multi-photon noise. Indeed to fully characterize this quantity one would require a deterministic splitting of the two (or more) photons paths and iterate the spitting for the idler photons. The sum of the two 4-fold accidental-coincidences events, which we measure, is in any case a good estimate for the different RR of our sources. Doubling the RR and simultaneously the average power, the ratio between the 4-fold accidental events and the double-pair events decreases: for $RR = [76, 152, 304, 608]$ MHz and corresponding power of $[120, 240, 480, 720]$ mW, the ratio results equal to $[0.75, 0.17, 0.10, 0.03] \pm 0.01$ %/mW, respectively. In other words, keeping the pair probability per pulse constant while increasing the RR results in a reduction of the accidental counts. In our data we see that the noise is decreased by over an order of magnitude by increasing the RR , while the pair-generation probability per pulse is kept to 0.01 at maximum pump power.

It is also possible to use our sources as heralded single-photon sources. In this case the important metric is the heralding efficiency. Normalizing for detector efficiencies, we measure heralding efficiencies of $[0.44, 0.56, 0.44, 0.52] \pm 0.02$ for signal and idler of Source 1 and Source 2, respectively.

4.2. Spectral analysis

Finding the correct crystal temperature is crucial to generate indistinguishable photon pairs with degenerate wavelengths. We record the full phase-matching temperature-tuning curves (see Appendix 5.2) using a poling period of $46.25 \mu\text{m}$ and choose a pump wavelength of 773.1 nm for the degenerate SPDC. At this pump wavelength, we set the crystal temperatures to 23°C for Source 1 and 24°C for Source 2. Due to the long wavelengths involved in the process, we require an accuracy of $\pm 1^\circ\text{C}$.

Using the single-photon spectrometer connected to a SNSPD, we first acquire the marginal single-photon spectra of both sources. For these data, only singles rate of the signal and idler photons are recorded. An example is shown in Fig. 3. Although these data do not reveal any information about the photons' correlations, they can be used to provide a rough estimate of the photon bandwidths, which are approximately $\sim 1 \text{ nm FWHM}$.

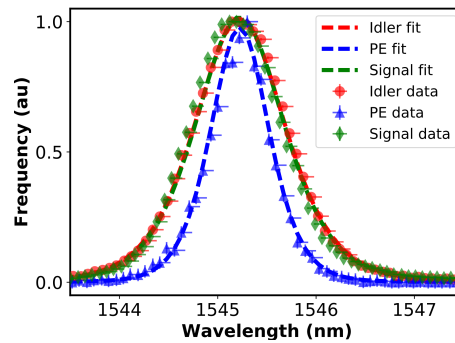


Fig. 3. Marginal spectra (red: signal and blue: idler) and pump envelope (PE) (green), recorded at 24 °C and with a pump wavelength of 773.1 nm. The pump-pulse width is set to (2.14 ± 0.02) ps. The FWHM of the signal, idler and PE spectra are 1.06 nm, 1.08 nm, and 0.70 nm, respectively. The central wavelengths of the spectra are shifted for an easy comparison of the shape and width of the spectral distributions.

Next we combine the two daughter photons into a single fiber, with the idler delayed with respect to the signal, and send them together to the spectrometer. We then connect the output fiber of the spectrometer to a fiber BS, splitting it into two fibers, and connect each fiber to a detector. Recording coincidence events between these two detectors, separated by the initial delay, allows us to collect an antidiagonal slice through the JSI function, which coincides with the pump envelope intensity. The antidiagonal spectrum is presented in Fig. 3, where it is evidently narrower than down-converted photons' spectra.

We then modify the width of the pump pulse and analyse the resulting variation of the photon bandwidths. We measure the pump laser's temporal width (using an interferometric autocorrelator) and the corresponding single-photon spectra, see Fig. 4. The relation between the pulse width and spectral width is governed by the time-bandwidth product, or, equivalently, by the Heisenberg uncertainty relation in time-energy [28]. Our measurement of this relation is indirect, as we have measured the pulse duration of the pump laser and the spectral width of the down-converted photons). Note that the idler photon has a slightly larger bandwidth than the signal photon, which is due to the fact that the direction of the phase matching intensity is not fully at 45° because the photons have different group velocities [14]. Similar data have been collected for the Source 2 and are reported in Appendix 5.3. The bandwidths of the idler photons of Source 1 and Source 2 behave slightly differently, revealing that the two processes are not fully identical. We believe this is mainly caused by the imperfections of the optical components present in the source, such as the inaccuracy in the poling periods of the two crystals or defects of the longpass filters (not shown in Fig. 1). The temporal multiplexing scheme does not influence the bandwidths of the photons (see Appendix 5.4 for details).

Changing the pump-pulse width will affect the spectral purity of the single photons. To study this, we use a second fiber-coupled single-photon spectrometer, allowing us to collect all the data required to reconstruct the JSI. Our second transmission-grating based scanning monochromator has a bandpass of 0.3 nm at 1550 nm and a scanning speed on the order of 1 nm/s. We report the results of these measurements for Source 1 and Source 2 together with our simulation of the JSI in Fig. 5. We observe a near-circular shape of the central JSI for Source 1 and Source 2. The experimentally extracted Schmidt numbers, the inverse of P_{JSI} , for Source 1 and Source 2 are 1.014 and 1.017 respectively, which are in good agreement with the simulated value of 1.012.

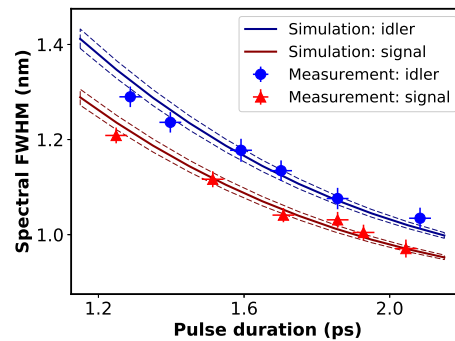


Fig. 4. FWHM of the marginal spectra in dependence of the pump-pulse width for Source 1. Solid lines are simulated values for signal (red) and idler (blue). The dashed lines represent the measurement uncertainty of the autocorrelator, ± 0.03 ps. The error bars of the data points show the uncertainty of the autocorrelator (in pulse-duration direction) and one standard error of the spectral distribution fit (in FWHM direction).

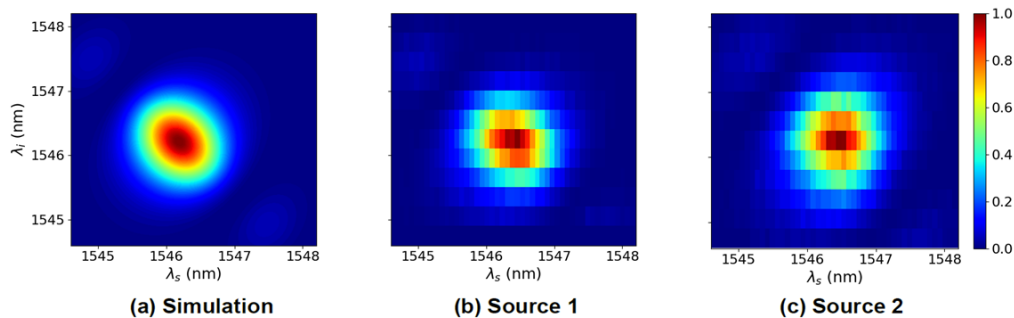


Fig. 5. Simulation (a) and experimental data of Source 1 (b) and Source 2 (c) of the joint spectral intensity. The measurements have been collected via two single-photon spectrometers. The Schmidt numbers calculated from these data are (a) 1.012, (b) 1.014, and (c) 1.017.

4.3. Quantum interference

We first perform HOM interference experiments between the signal and idler photons of the two individual sources, obtaining almost ideal visibilities. An example interference plot with a visibility of 99.1 ± 0.2 % is shown in Appendix 5.5. This corresponds to a high indistinguishability, which is consistent with our JSI results. This type of interference is highly dependent on the crystal temperature, because tuning the temperature away from our design temperature leads to a non-degenerate SPDC process. Here the HOM interference measurements show a fringe pattern within the dip, which has been called “quantum beating” [29]. Further details and data can be found in Appendix 5.6.

To complete our correlation analysis, we perform a HOM interference experiment between the signal photons from our two different sources, heralded on detection of the two idler photons. The analysis of the multi-photon noise is performed following the same procedure as described in Section 4.1. In Fig. 6 we show in green the data of the polished 4-fold coincidences and in grey the data of the partial multi-photon noise. We find a maximum visibility of 0.80 ± 0.02 at a pump power of 60 mW and $RR = 76$ MHz, after subtracting the accidental-coincidence events. The coherence length of the two photons, obtained by the width of the HOM dip, is equal to

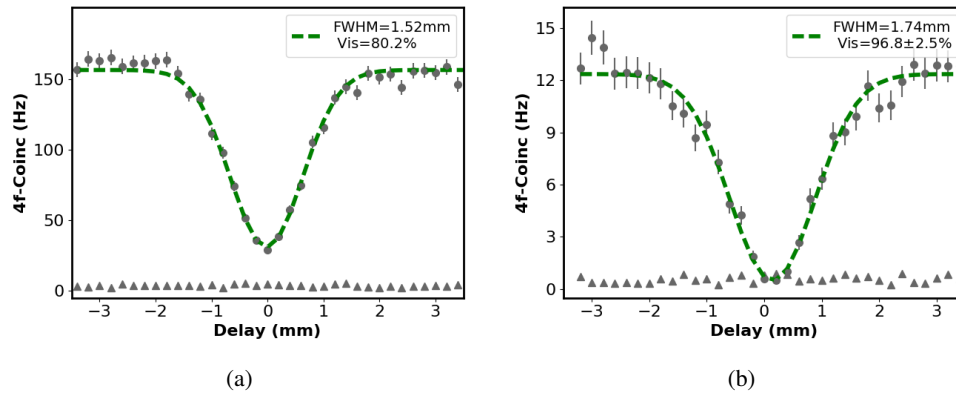


Fig. 6. HOM interference between signal and signal photons of the two independent sources without (a) and with narrow-bandpass filters (b). The 4-fold accidental coincidences are shown with the grey triangles at the bottom and have been subtracted to calculate the shown visibilities. The error bars are calculated from Poissonian counting statistics.

(1.52 ± 0.04) mm (see Fig. 6(a)).

We repeat these tests for different pump-pulse widths in order to optimize the purity of the single photons by matching the pump-pulse width to the phase-matching bandwidth. As seen in Fig. 7, the visibility changes by more than 10% by fine tuning the pulse width.

Using our multiplexing scheme, we repeat these measurements for various repetition rates and pump power. These data are shown in Fig. 7(b). We find that for higher RR we are able to increase the pump power significantly, and still obtain the same spectral purity. This demonstrates that our multiplexing greatly mitigates the effects of higher-order emissions, allowing us to maintain good spectral purities even at high count rates.

The maximum purity, calculated from the JSA simulation for our experimental source parameters, is about 0.82, due to the presence of the JSA side lobes (partially visible also in the JSI, see Fig. 5). Experimentally, the raw maximum purities correspond to $[0.78, 0.77, 0.77, 0.78] \pm 0.02$ for $RR = [76, 152, 304, 608]$ MHz, respectively. The discrepancy between our simulation and experimental results is mainly due to the inaccurate poling periods and the imperfect optical components inserted in the photons path.

4.4. Photon filtering

Further enhancement of the spectral purity can be achieved through spectral filtering, which removes the side lobes of the JSA. This comes at the cost of reducing the brightness [7]. We use filters of nearly top-hat shape with a central wavelength of 1545 nm and a FWHM of 3.2 nm and an average central peak transmittivity of 97%. As the FWHM of our signal and idler photons is about 1 nm, ideally we would use narrower filters, but the broader filters allow us to study variations in the purity and brightness. They also offer the ability to tune the single-photon source wavelength according to the chosen application. For a specific JSI, changing the central wavelength of the filters selects different sides of the JSI, and affects both the visibility and the photons loss. Changing the pump wavelength, while keeping the filters fixed, leads to the same outcome. We simulate the four-fold HOM visibility, while scanning the pump wavelength, such that the daughter photons' wavelengths cover the entire bandpass of the filters, see Fig. 8. We consider two filters (2F) (one on each of the signal photons) and four filters (4F) (one on each

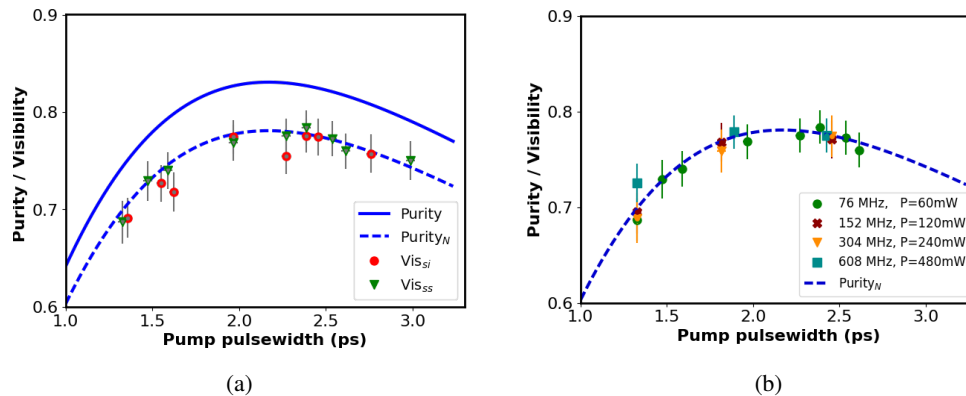


Fig. 7. Experimentally measured HOM visibility (which is, ideally, the same as the spectral purity) for different pump-pulse widths. (a) Data collected at a laser $RR = 76$ MHz and constant pump power of 60 mW. The solid blue curve is the simulated visibility. The dashed curve is the same simulation including a noise factor (to explain technical imperfections), which fits the experimental data well. (b) Data collected for different repetition rates and increasing pump powers. The dashed curve is normalized simulated purity, including the same noise factor. In both figures the background from accidental counts was not subtracted.

signal and each idler photon). In addition, we compute: the total loss of the 4-fold coincidence rate with respect to the no filter case (L_{tot}); the loss of the 4-fold coincidence rate originating from the indistinguishable photons, corresponding to the central peak of the JSI (L_{\odot}); and the residual amount of unwanted 4-fold coincidence contributions due to the JSA side lobes (R). The filter profiles were approximated by a rectangular function with 100% transmittivity. As shown in Fig. 8, one must find an appropriate trade-off between the increased visibility and photon losses caused by the filters. For example, for experiments where it is not required that all photons interfere with each other, two filters could be preferable, whereas achieving ultra-high purities requires a filter for each photon. It is worth noting that when the visibility (blue line) decreases the residual amount of unwanted photons (green line) increases and vice versa, underlining that only the side-lobes are affecting the purity (for a zoomed plot see Appendix 5.7). Also, the total loss (orange line) for the central range is mainly composed of losses from unwanted distinguishable photons, which usually contribute to the brightness.

We experimentally acquired the 4-fold HOM visibility for the two and four filter cases at different wavelengths within the bandwidth of the filters. The results, along with the simulations, are shown in Fig. 9(a). In addition, the experimental loss compared to the initial 4-fold coincidence rate is shown in Fig. 9(b). We find a 10% improvement in the visibility with respect to the no-filter case with two filters on the two interfering signal photons, and an overall loss of approximately 20% to the 4-fold coincidence rate (see Appendix 5.8 for the single-filter losses). For the 2F case, tuning the pump wavelength further, and consequently introducing more losses, does not enhance the photon purity because of the relatively large filter bandpass. On the other hand, inserting additional filters on the heralding idler photons enables us to reach a maximum visibility of 0.97 ± 0.03 (Fig. 6(b)), although this comes at a cost of an almost $\sim 80\%$ loss to the 4-fold coincidence rate. At the other end of the curve, the 4-fold coincidence rate is reduced by 35% to achieve 92% visibility. The high loss originates from a non-ideal transmittivity, a non-perfect top-hat shape, and a central wavelength mismatch (of about 0.2 nm) between the filters. The imperfect visibility can be explained by a combination of: imperfect splitting ratios and polarization drift of the fiber-tunable beam splitter; additional short fibers and free-space

delay stage for the photons synchronization; and the small differences between each filter.

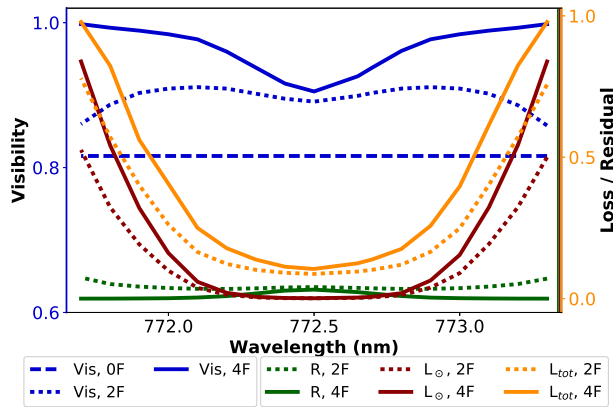


Fig. 8. Simulation of 4-fold HOM visibility and different losses when using no filters (dashed curve), 2 filters (dotted curves), and 4 filters (solid curves). Blue: 4-fold HOM visibility. Orange: total loss of 4-fold coincidences caused by the filters. Red: Loss of 4-fold coincidences originating from the central peak of the JSI. Green: Residual contributions of the side lobes of the JSI to the 4-fold coincidence events.

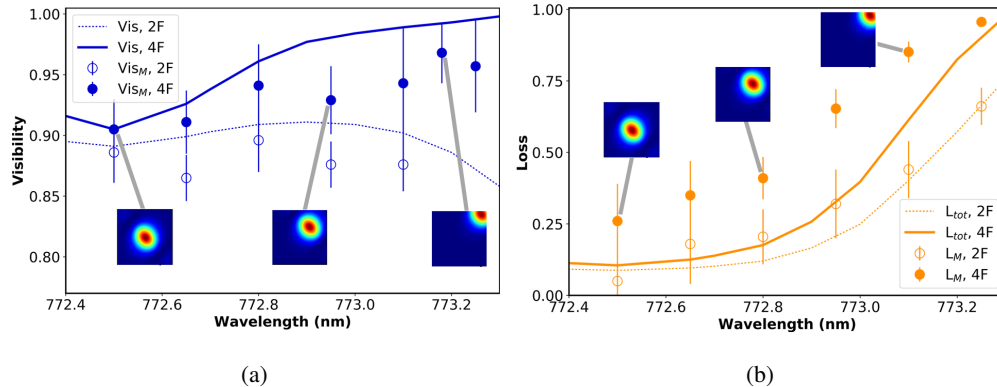


Fig. 9. Simulation and measurement data for of the HOM visibility (a) and total filter losses (b). The subfigures show the effect of 2 filters on the JSI at the corresponding wavelength. Note that all the curves here refer to the 4-fold coincidence events.

5. Conclusion

We have presented a complete characterization of two ppKTP-SPDC sources to create telecom-wavelength photons. By tuning the laser pump-pulse width and the laser repetition rate we optimized the purity of the single photons while maintaining a high source brightness. We found that the pump-pulse width contributes significantly to the quality of the down-converted photons.

We used the complementary measurements of the JSI and HOM interference to characterize two independent down-conversion sources, finding a configuration resulting in high indistinguishability and purity for both sources.

Our single-photon spectrometer, fiber-coupled at the input and output, and our super-conducting nano-wire single-photon detectors were crucial in the optimization of our single-photon sources. Additionally, using narrow-bandpass filters on either two or all four photons enhanced the spectral purity up to 0.90 and 0.97, respectively, at the cost of photon count rates. We found an optimal case using four filters, wherein we achieve a purity of 0.94 and still maintain a high brightness of 2.2 kHz/mW. However, for applications wherein high purity is indispensable, we can obtain a purity of 0.97, by reducing the brightness to 1.1 kHz/mW.

Tuning several variables of the single-photon sources allowed us to perform an in-depth study of the down-converted photons, highlighting the importance carefully designing and fabricating single-photon sources. We believe our work can be used as a guide to realize practical telecom single-photon sources.

APPENDIX

5.1. Detector-independent single-photon spectrometer

The in-house built single-photon scanning monochromator in use is based on a planar diffraction grating and off-axis parabolic mirrors in a Z-configuration. It is single-mode fiber coupled for detector independence and has a resolution of 0.12 nm. A piezoelectric motor is used as rotation stage which, together with the use of off-the-shelf optics, keeps the cost low. The control software is able to acquire data from an AIT TTM8000 time tagging module, which acts as an interface to any detector providing a digital signal. Spectral coincidence measurements can be carried out between two channels of the TTM8000. Compared to the common approach of building a spectrograph utilizing the chromatic group velocity dispersion of tens of kilometers of optical fiber, this grating based monochromator offers a higher efficiency (up to 0.3 for this specific device, whereas a usual fiber-spectrograph requires 50 km of fiber with a resulting efficiency of 0.1 to reach 0.12 nm of resolution [30]).

5.2. Phase-matching curve

We report in Fig. 10 an example of a phase matching curve acquired for Source 1. The ppKTP crystal is fabricated for degenerate SPDC 775 nm \rightarrow 2 \times 1550 nm with poling period of 46.2 μ m. We simulate the process considering the Sellmeier equations from [31, 32], coefficients for both thermal expansion and thermo-optical effect from [33] and a poling period of 46.25 μ m to match the experimental observations.

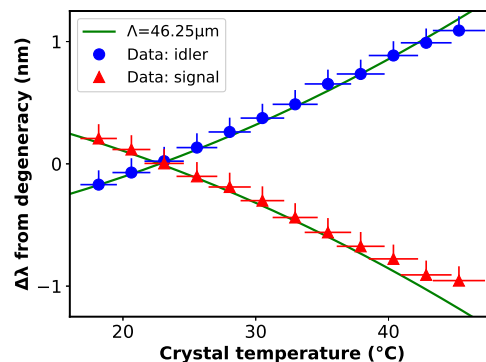


Fig. 10. Phase matching curves for two down-converted photons, idler and signal, generated in a ppKTP crystal of 30 mm length. The green lines represent the simulated curves for a periodic poling of 46.25 μ m.

5.3. Time-energy relation between pump and daughter photons

Due to the time-energy uncertainty principle the spectral distribution of a pulsed laser is of finite width, and so are the marginal spectra in a pulsed SPDC-source. The relation between temporal and spectral width of the pulse reads $\Delta\tau\Delta\sigma = \text{TBWP}$ for fourier-limited pulses, with the pulses temporal width $\Delta\tau$, its spectral width $\Delta\sigma$ and the time-bandwidth product TBWP, which is $((2 \log(1 + \sqrt{2})) / (\pi))^2 \approx 0.3148$ for sech^2 pulses. Variations of the temporal width of the pump, and thus of the pump envelope amplitude, change the FWHM of the daughter photons as the marginal spectra are the projection of the JSI onto the respective axis. The change of the marginal FWHM in dependence of the pump temporal width was shown in the main text for Source 1 and here for Source 2, see Fig. 11.

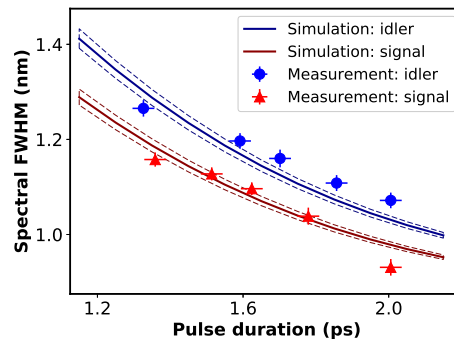


Fig. 11. FWHM of the marginal spectra in dependence of the pump-pulse width for Source 2. Solid lines are simulated values for signal (red) and idler (blue). The dashed lines consider the measurement uncertainty of the autocorrelator, ± 0.03 ps. The error bars of the data points show the uncertainty of the autocorrelator (in pulse-duration direction) and one standard error of the spectral distribution fit (in FWHM direction).

5.4. Spectral analysis of multiplexing

Spectral FWHM measurements of the daughter photons have been carried out to verify that the use of the temporal multiplexing scheme does not influence the marginal spectra. The results can be seen in Fig. 12. We find that the daughter photons FWHM are unaffected by the repetition rate.

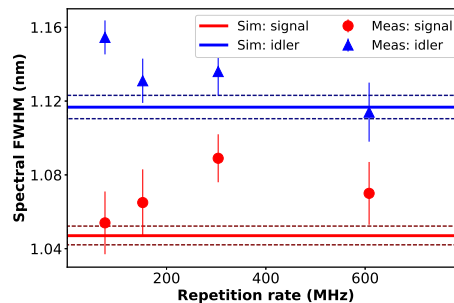


Fig. 12. FWHM of signal and idler photons at different steps of the passive temporal multiplexing scheme. The error bars show one standard error of the spectral distribution fit. The uncertainty band of the simulation accounts for the uncertainty of the pulse width measurement using the autocorrelator.

5.5. Indistinguishability

Quantum interferences between down-converted photons generated from the same source are analysed for the two sources without any additional bandpass filter (Fig. 13). High visibilities, till 99.5%, demonstrate the intrinsic indistinguishability arising from the quasi-phase matching and group velocity matching of the SPDC process. The particular V-shape of the HOM dip, due to the group velocity matching of type II down conversion, is evidently appearing since no bandpass filters are present.

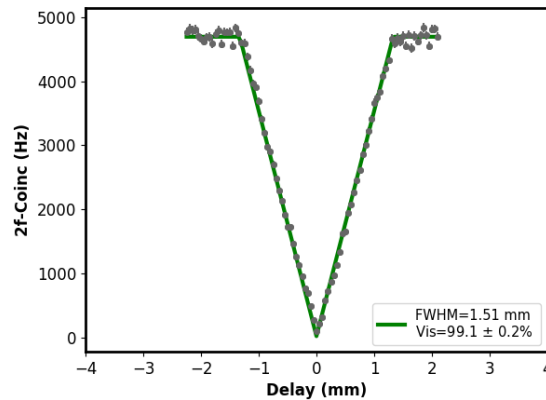


Fig. 13. HOM dip between signal and idler from the same source.

5.6. Quantum beating

HOM interference measurements are shown in Fig. 14 for photon pairs generated by one ppKTP-SPDC process at different crystal temperatures. Varying the temperature detunes the central wavelengths of the two photons within the non-degeneracy (see Fig. 10). The more the wavelengths are apart, the bigger the number of beats which appear within the HOM dip. This can be explained by the various phases owned by the photons at different wavelengths, as in the JSA. The effect describes a hidden-frequency entanglement [29].

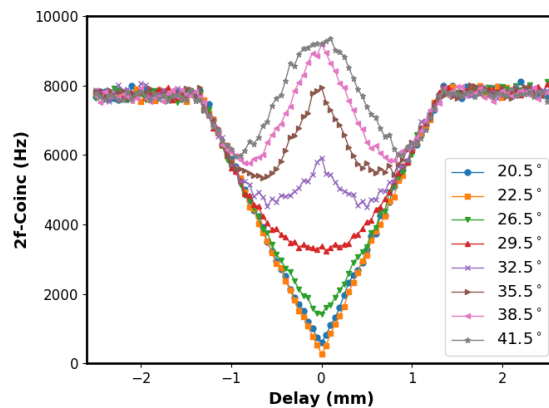


Fig. 14. HOM interference for different crystal temperatures, corresponding to a wavelength detuning of the down-converted interfering photons. Only raw data are reported.

5.7. Filters simulation

In Fig. 15 we report singularly the behaviours of the photons purity and the photons losses for the case of filtered photons. A symbolic representation of the plotted quantity is shown on the right of each graph.

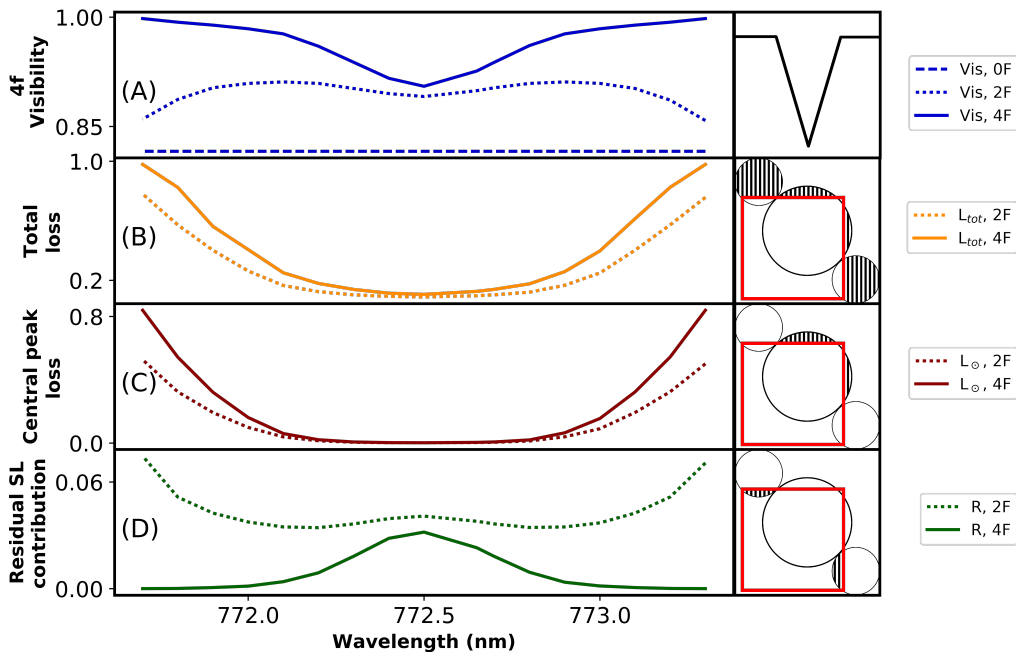


Fig. 15. Simulation of 4-fold HOM visibility and different losses when using no (dashed curve), 2 (dotted curves), and 4 filters (solid curves). (A): 4-fold HOM visibility. (B): total loss of 4-fold coincidences caused by the filters. (C): Loss of 4-fold coincidences originating from the central peak of the JSI. (D): Residual contributions of the side lobes of the JSI to the 4-fold coincidence events. For (B-D), the second column holds sketches visualizing the effect of two filters on the JSI. The dashed area corresponds to the plotted curve.

5.8. Filtered photons loss

The total losses related to the single-photon event, per narrow-bandpass filter, are shown in Fig. 16, together with the simulation. For the simulated case we consider a filter with 100% transmittivity and a rectangular-shape transmission profile. In practice the filters do not fully coincide with the ideal case. This explains the divergence of the data and the simulation.

One filter presents a deviation of the central wavelength (CW) of 0.2 nm with respect the CW of the other filters. The imperfection causes additional losses, which result significant for the single photons.

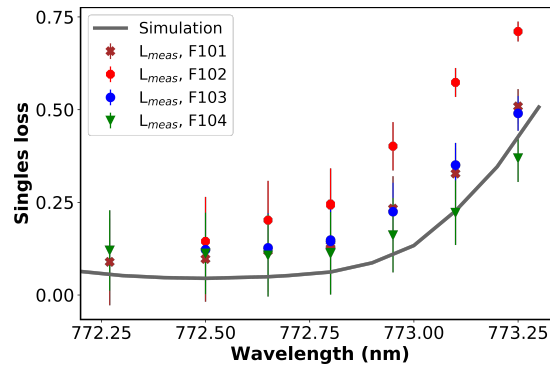


Fig. 16. Loss of single-event rate introduced by narrow-bandpass filters, both measured (dots) and simulated (curve). Filter F102 exhibits a higher loss than the other filters because its central wavelength is shifted by 0.2 nm with respect to the others. The simulation is underestimating the losses due to the chosen rectangular function as filter transmission profile and unity-transmittivity.

Funding

European Commission through EQUAM (No. 323714), PICQUE (No. 608062) and QUCHIP (No. 641039); Austrian Science Fund (FWF) through START (Y585-N20), the doctoral programme CoQuS (W1210) and NaMuG (P30067-N36); United States Air Force Office of Scientific Research via QAT4SECOMP (FA2386-17-1-4011).

Acknowledgments

We thank Max Tillmann, Fabian Laudenbach, Amir Moqanaki and Francesco Massa for useful discussions. We acknowledge the AIT institute for lending one single-photon spectrometer for the JSI measurements and the simulation software QPMoptics [34] for a comparison of our simulations. L.A.R. acknowledges support from the Templeton World Charity Foundation (fellowship no. TWCF0194).